ChemPubSoc Europe
DOI: 10.1002/slct.201900584
ChemistrySELECT Full Papers

Energy Technology & Environmental Science

Flute-like Fe_2O_3 Nanorods with Modulating Porosity for High Performance Anode Materials in Lithium Ion Batteries

Huanqing Liu, Jiajia Zou, Yanhua Ding, Tuo Xin, Bing Liu,* and Yiqian Wang*[a]

Flute-like Fe_2O_3 nanorods with tunable porosity are obtained by facile hydrothermal process and subsequent calcination. The morphology, porosity and structural stability of Fe_2O_3 nanorods are effectively controlled by a two-step strategy at nano/micrometer scale. The introduction of F ions promotes the formation of nanorod-like iron hydroxide precursors, which are annealed at 400, 500 and 600 °C to obtain Fe_2O_3. The pore size increases with the annealing temperature. When tested as anode material of lithium ion batteries (LIBs), the porous Fe_2O_3 nanorods obtained by annealing at 500 °C exhibit better cycling stability and rate capability than those obtained at 400 and 600 °C. Most impressively, it delivers a capacity of 707.4 and 687.7 $mAh\,g^{-1}$ at 1 and 2 A g^{-1} after 200 cycles, respectively. Compared to the other two samples, the Fe_2O_3 nanorods with optimized pore distribution exhibit robust porous framework, which contributes to the structural and electrochemical stability of electrode. The porous framework can effectively alleviate the severe volume expansion/contraction and avoid pulverization of active materials, resulting in outstanding reversibility and rate capability. This work will benefit the design of novel materials for LIBs.

Introduction

Driven by the demand of new energy vehicles and stationary storage systems, high-performance batteries have attracted increasing attention.[1–4] Lithium ion batteries (LIBs) have become competitive candidate of most electric vehicle companies, including Tesla, Toyota, BYD, *etc.*, due to their high energy density, high working voltage, long lifespan and environmental geniality.[5,6] However, current commercial graphite-based anode materials (372 $mAh\,g^{-1}$) are far from satisfying the actual demand for high energy density. The past decades have witnessed much progress toward advanced electrode materials, especially in transition metal oxide materials.[7,8] Among the transition metal oxides, hematite nanomaterials have been considered to be promising anode materials because of their high theoretical capacity (arising from conversion reaction with lithium), low cost, natural abundance and environmental friendliness. Despite these distinct advantages, Fe_2O_3 electrode always suffers from poor cycle ability caused by the dramatic volume changes during charge/discharge processes, which hinders its application in LIBs.[9–11]

To overcome the intrinsic disadvantages of Fe_2O_3, intensive efforts have been devoted to the fabrication of novel micro/nano-structures and synthesis of various nanocomposites. In particular, the fabrication of porous structural electrodes has proven to be a suitable strategy for LIBs.[12–26] Recently, many studies have reported the synthesis of Fe_2O_3 with hierarchical porosity and unique microstructure, such as hollow spheres and cubes,[14,15] Fe_2O_3@N–C hollow nanoparticles,[16] hollow nanobarrels α-Fe_2O_3/rGO,[17] 3DG/Fe_2O_3 aerogel,[18] 3D hierarchical porous α-Fe_2O_3 nanosheets,[19] and porous Fe_2O_3@C rods.[20] Sun et al. reported that porous Fe_2O_3 nanotubes could deliver a charge capacity of 951.6 mA h g^{-1}, which is much higher than that of Fe_2O_3 nanoparticles.[21] The porous nanostructure provides a larger surface area than that of non-porous systems. High surface area ensures effective contact between electrolyte and electrode surface, and promotes charge transfer across the electrode-electrolyte interface.[22–24] In addition, vacancies in porous nanostructure buffer the volume changes associated with electrochemical reactions, thus ensuring the structural stability in the cycling process.[25–26] Therefore, the introduction of a large number of pores into the electrode material is an important factor in determining the superior rate capability and long cycle stability of the battery. To fabricate optimized porous Fe_2O_3 anode by modulating porosity represents a promising opportunity towards high-performance LIBs.

Herein, three flute-like porous Fe_2O_3 samples were obtained by annealing the precursor at 400, 500 and 600 °C. As the annealing temperature increases, the pore size increases. The porous Fe_2O_3 nanorods with appropriate size distribution show better cycle stability and rate capability, compared to the samples obtained at 400 and 600 °C. The improved lithium storage performance can be attributed to stable structure of the materials and the appropriate void ratio. On one hand, the robust porous framework contributes to the structural stability of electrode during electrochemical cycling. On the other hand, the Fe_2O_3 nanorods possess large pore volumes and surface areas, which provides sufficient space to accommodate volume change and promote ion transport.

[a] *H. Liu, J. Zou, Y. Ding, T. Xin, Dr. B. Liu, Prof. Y. Wang*
College of Physics and State Key Laboratory, Qingdao University, No. 308 Ningxia Road, Qingdao, 266071, China
E-mail: bing_liu@qdu.edu.cn
yqwang@qdu.edu.cn

Supporting information for this article is available on the WWW under https://doi.org/10.1002/slct.201900584

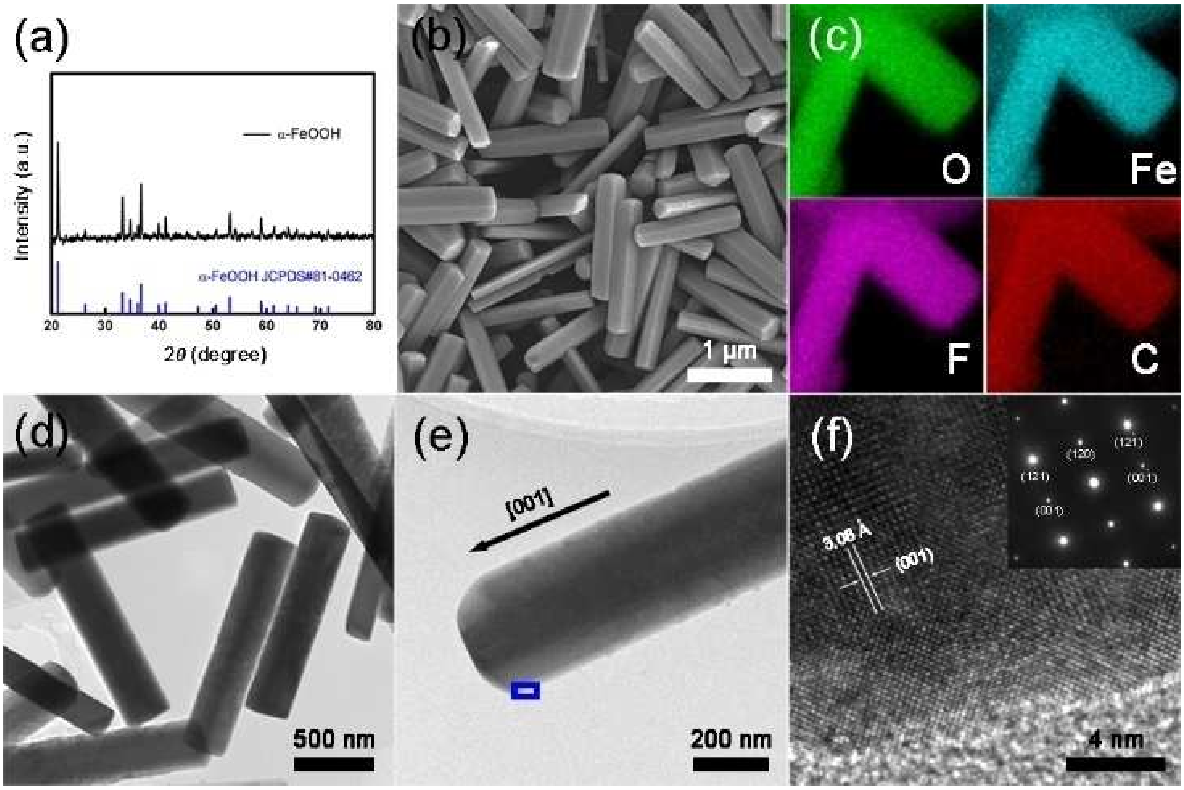

Figure 1. (a-c) XRD pattern, SEM image and element mapping of precursors. (d-e) typical TEM images of precursors. (f) HRTEM image taken from (e). Inset in (f) is the corresponding SAED pattern.

Results and Discussion

The Fe_2O_3 nanorods with tunable porosity were prepared by direct calcination of the precursors in air at different temperatures (see Supplementary Information for more experimental details). The phase of the precursors was identified as orthogonal α-FeOOH by X-ray powder diffraction (XRD) (Figure 1a).[27] The morphology of the as-prepared precursor was characterized by scanning electron microscopy (SEM) and transmission electron microscopy (TEM). Figure 1b shows the SEM image of the sample, from which it can be seen that the precursors possess a rod-like shape with widths of 150–250 nm and lengths of 1.2-1.5 μm. The elemental mapping (Figure 1c) confirms the uniform distribution of Fe and O elements in the sample. The F and C elements are also found, which might be introduced by the initial agents. Furthermore, the X-ray photoelectron spectroscopy (XPS) spectrum of the precursor also confirms these features (Figure S3).[28,29] The TEM images (Figure 1d and e) also show distinct rod-like structure. The high-resolution TEM (HRTEM) image in Figure 1f is taken from the region enclosed by a blue rectangle, which reveals that the growth direction of the precursor is along [001]. Inset in Figure 1f is the corresponding selected-area electron diffraction (SAED) pattern, which indicates that the precursor is α-FeOOH. Interestingly, in the same reaction system, cubic Fe_2O_3 could be directly synthesized without adding of NH_4F, which was confirmed by XRD and SEM (Figure S1 and S2). Under hydrothermal condition, $Fe(OH)_3$ colloid was firstly produced by hydrolysis of Fe^{III}. Without the addition of F^-, the Fe_2O_3 nanocrystal was synthesized through the dehydration of $Fe(OH)_3$. The introduction of F^-can enhance the structural stability of FeOOH, which contributes to the transformation from $Fe(OH)_3$ to FeOOH. In addition, the existence of F^- increases the polarity of the solution, which is conducive for FeOOH nanocrystals to grow along one-dimensional direction and finally become rod-like FeOOH. Therefore, the introduction of F^- changes the phase of the resultant products and the morphology of nanostructures.

Three samples obtained by annealing at 400, 500 and 600 °C were referred to as Fe_2O_3-400, Fe_2O_3-500 and Fe_2O_3-600, respectively. Figure 2 shows the XRD patterns obtained from the three samples, where all the diffraction peaks can be indexed to rhombohedral phase Fe_2O_3 (JCPDS No.: 87–1166).[30] No other peaks were found, indicating that the as-synthesized iron hydroxide was completely converted to Fe_2O_3 after annealing in air at 400 °C. In addition, the intense and sharp diffraction peaks suggest that the crystallinity increases with annealing temperature. Based on the thermogravimetric analysis (TGA) (Figure S4), iron hydroxide can be converted to Fe_2O_3 at about 400 °C and the mass remains unchanged after 500 °C.

The chemical composition of Fe_2O_3-500 was determined by XPS. Figure 3a shows distinct Fe, O and C element peaks, and weak F element peak. The small amount of residual F^- might result from the electrostatic interaction between F^- and Fe^{3+}.

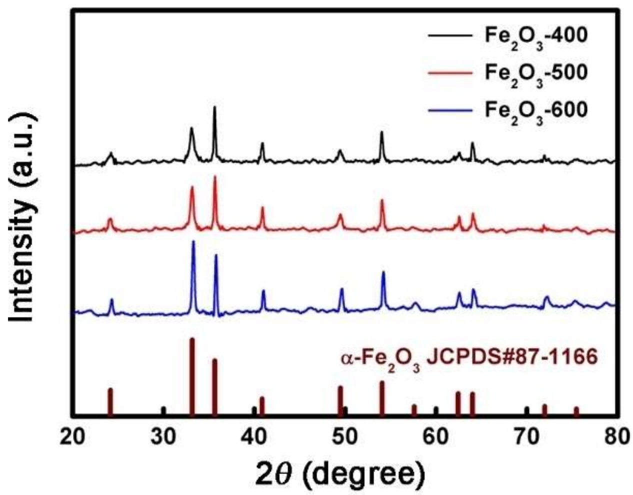

Figure 2. XRD patterns of annealed product at different temperatures.

The peaks at 710.9 and 724.6 eV in the Fe 2*p* spectrum belong to Fe $2p_{3/2}$ and Fe $2p_{1/2}$, respectively.[31] Besides, satellite peaks are also observed at side of the main peaks, which confirms the existence of Fe^{3+}.[32] Figure 3c displays the specific spectrum of O 1s. The binding energy peaks centered at 529.9 and 531.7 eV can be assigned to O^{2-} binding and C–O binding.[33] In the spectrum of C 1s, the peak at 284.8 eV corresponds to sp^2 bond (C–C) of the carbon, suggesting the carbonization of residues. These results further confirm the existence of α-Fe_2O_3.

The morphology and structure of Fe_2O_3-500 sample were examined by SEM and TEM. It can be seen from SEM image (Figure 4a) that Fe_2O_3-500 shows flute-like nanorod shape with diameter of 100–250 nm. The low-magnification TEM image of the product (Figure 4b) clearly shows the porous structure and a large number of mesopores were observed in all visible nanorods. The enlarged TEM and HRTEM images indicate the existence of cavity and porous wall (Figure 4c and d). The lattice spacings of 2.87 Å corresponds to the $(20\bar{2}0)$ lattice planes of Fe_2O_3, suggesting that the long axis direction of the nanorod is along $[10\bar{1}0]$.[34]

The corresponding SAED pattern reveals the single-crystalline nature of α-Fe_2O_3, which is highly consistent with the XRD results. The formation of mesopores can be attributed, on the one hand, to the dehydration and recrystallization during phase transformation, and on the other hand, to the loss of large amounts of organic groups in the FeOOH precursor

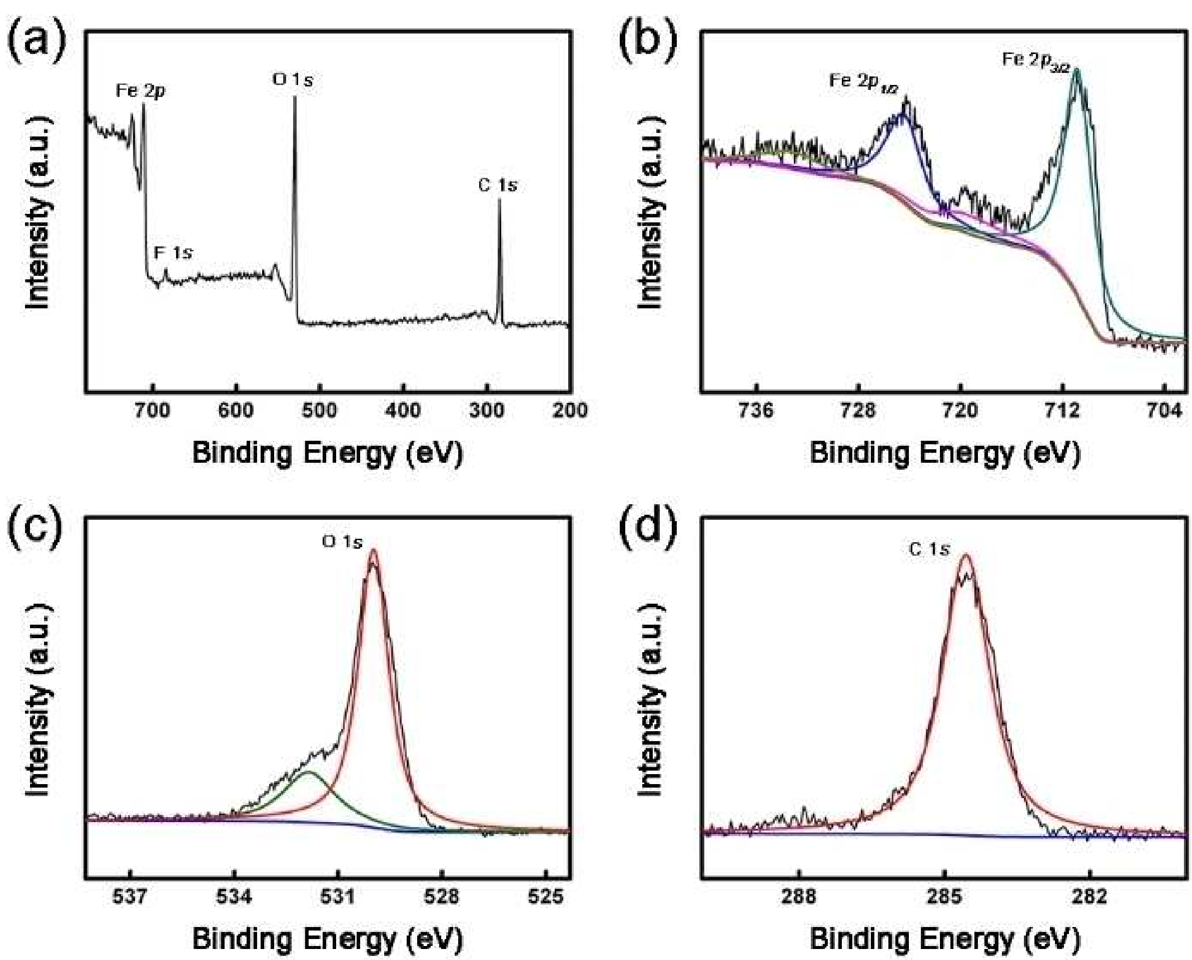

Figure 3. XPS spectra for the Fe_2O_3-500. (a) full scan; (b) Fe 2*p*; (c) O 1s; (d) C 1s.

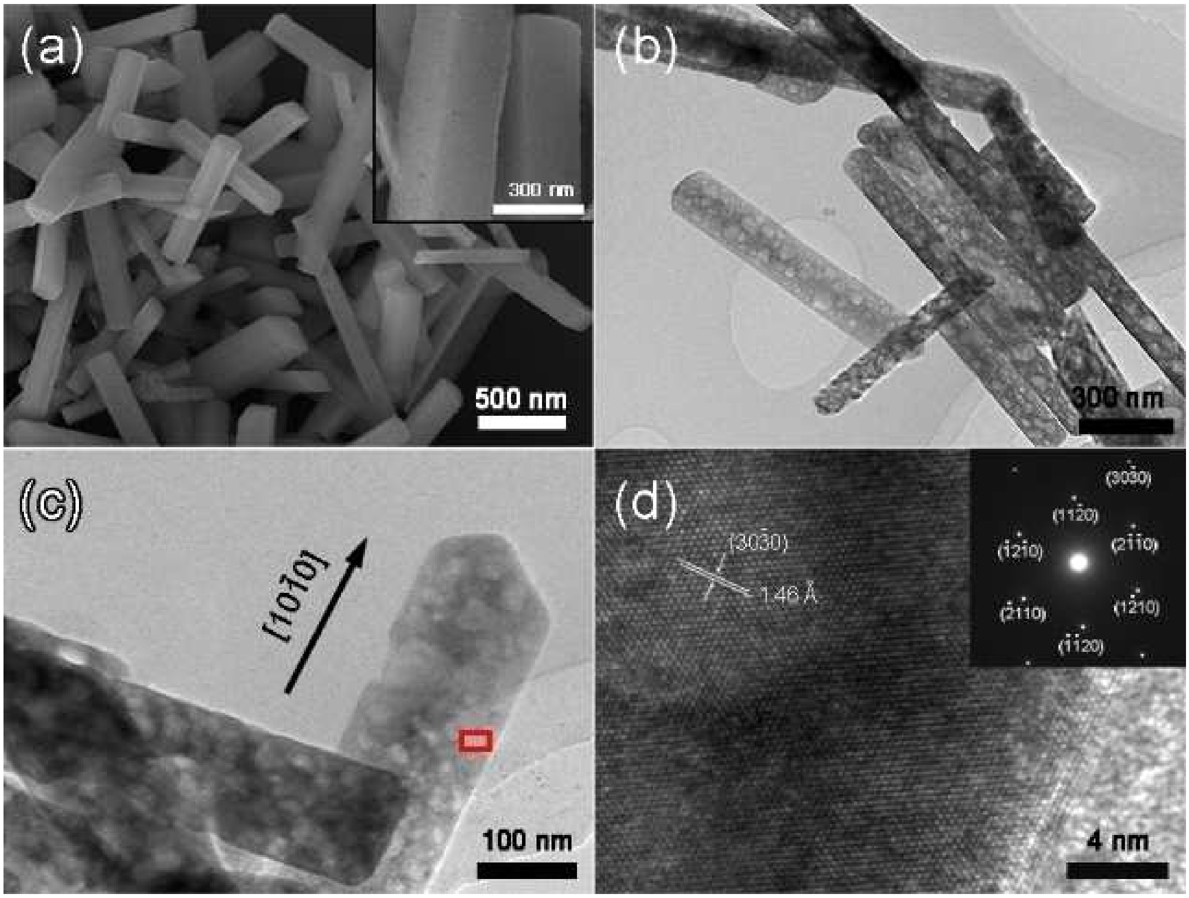

Figure 4. (a) Typical SEM image of Fe_2O_3-500, inset is magnified SEM image. (b, c) Bright-field (BF) TEM images of Fe_2O_3-500. (d) HRTEM image taken from the region enclosed by a red rectangle, inset is the corresponding SAED pattern.

during annealing process. The robust porous framework with large pore volumes and surface areas contributes to the structural stability and rapid ion transport.

To verify the porous structure, the morphology of three samples was examined by SEM. As can be seen from Figure 5, both Fe_2O_3-400 (Figure 5a and b) and Fe_2O_3-600 (Figure 5g and h) are rod-like shape, which are similar to Fe_2O_3-500 (Figure 5d and e). The enlarged SEM images show the visible holes on the surface after calcination at 500 °C. As the annealing temperature increases to 600 °C, the size of holes is maximized and the framework of the nanorods becomes unstable. The result is also confirmed by the nitrogen adsorption-desorption isotherms and the corresponding pore size distribution. As shown in Figure 5(c, f and i), these isotherms can be identified as type IV, which is characteristic of mesoporous materials.[35] The moderate Brunauer-Emmett-Teller (BET) specific surface area of Fe_2O_3-400 was found to be 27.59 $m^2 g^{-1}$, which was higher than that of Fe_2O_3-500 (18.24 $m^2 g^{-1}$) and Fe_2O_3-600 (9.33 $m^2 g^{-1}$). According to its pore size distribution curve (inset in Figure 5c), the predominant pore size obtained using the Barrett-Joyner-Halenda (BJH) method was 3.7 nm. The Fe_2O_3-500 sample shows three main pore sizes of 3.9 nm, 7 nm and 14 nm, respectively. Consistent with SEM images, the Fe_2O_3-600 sample has a larger pore size, mainly distributed at 3.8 nm, 7.8 nm and 30 nm. However, the material annealed at 500 °C has a maximum pore volume of 0.21 $cm^3 g^{-1}$ than that of Fe_2O_3-400 (0.114 $cm^3 g^{-1}$) and Fe_2O_3-600 (0.087 $cm^3 g^{-1}$).

To further investigate the porous nature, the TEM images of three samples were recorded in Figure 6.

As can be seen, dense holes were found among three samples. With the increase of annealing temperature, the pore size increases. In addition, some Fe_2O_3-600 nanorods were found to be broken due to the formation of large holes, which in turn caused structural instability. To give a reliable distribution of pore size, a statistical analysis of the pore size was carried out and more than 100 nanorods in each sample were measured. Figure 6(c, f and i) shows the pore-size distributions of Fe_2O_3-400, Fe_2O_3-500 and Fe_2O_3-600, respectively. Obviously, the Fe_2O_3-500 sample exhibits a relatively wider pore size distribution from 3 to 22 nm and there is a dominant group with a diameter of about 7 nm, compared to the Fe_2O_3-400 sample (2-7.6 nm). As the annealing temperature increases, the pore tends to merge and pore size continues to increase. The pore size of Fe_2O_3-600 sample ranges from 2 to 77 nm in diameter. It is believed that the proper porous structure can alleviate the volume changes effectively and facilitate ion transport during charge/discharge processes. The Fe_2O_3 nanorod obtained at 500 °C possesses larger pore volume and stable

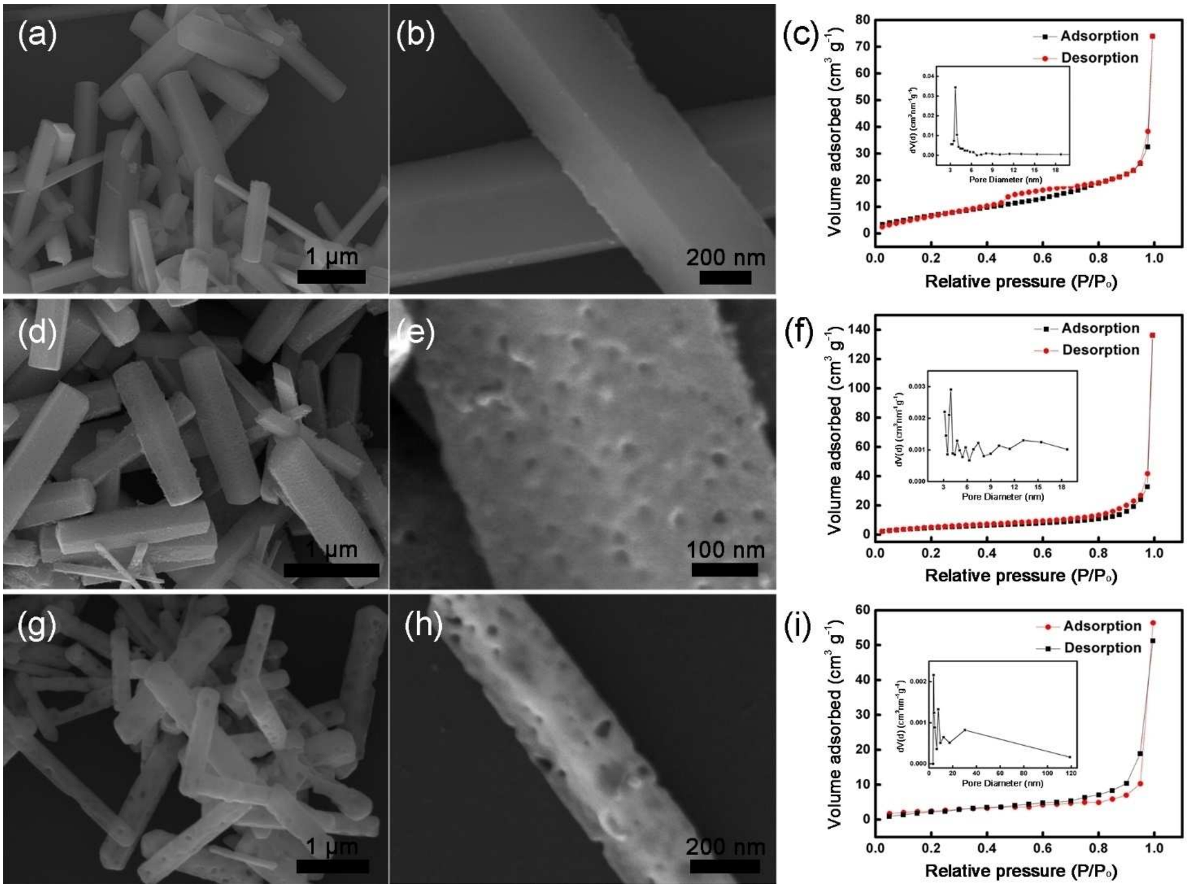

Figure 5. Typical SEM images and Nitrogen adsorption-desorption isotherms of (a-c) Fe_2O_3-400 nanorods, (d-f) Fe_2O_3-500 nanorods, and (g-i) Fe_2O_3-600 nanorods.

porous framework, which contribute to the improved lithium storage performance.

The electrochemical performance of the Fe_2O_3-500 electrode was evaluated, and the other Fe_2O_3 samples were also tested for comparison. Figure 7a shows the cyclic voltammetry (CV) curves collected between 0.01 and 3.0 V. A strong cathodic peak at 0.39 V was detected in the first cycle, which corresponds to the reduction of iron from Fe^{III} to Fe^0 and the formation of a solid electrolyte interphase (SEI) layer.[36] During the anodic process, a broad current peak at 1.75 V corresponds to the oxidation of Fe^0 to Fe^{II} and then to Fe^{III}.[37] The overlapping of the CV curves in the following cycles reveals good reversibility of the electrochemical reactions, which can be further demonstrated by the cycling performance. However, the CV curves of cubic Fe_2O_3 show that the peak intensity gradually decreases, suggesting that the reversibility is not good (Figure S5). Figure 7b shows the initial charge/discharge profiles of annealed samples at a current density of 200 mA g^{-1}. The initial discharge and charge capacities of Fe_2O_3-500 are 1210 and 877.5 mAh·g^{-1}, and the irreversible capacity loss can mainly be assigned to the formation of the SEI layer.[21] The initial Coulombic efficiency (CE) was measured to be 72.5%, which was higher than the value of 68.5% for Fe_2O_3-400 and 71.3% for Fe_2O_3-600. During the first cycle, irreversible side reactions take place on the electrode surface. The large specific surface area may lead to more side reactions, which is responsible for low CE of Fe_2O_3-400.[38] Moreover, it can be seen from Figure 7c that the capacity of the Fe_2O_3-500 electrode ranges from 981 to 939 mAh g^{-1} between the second and 50th cycle, and no obvious decay is observed.

Figure 7d shows the cycling performance of three annealed samples. Obviously, the Fe_2O_3-500 exhibits higher specific capacity and better stability in the three samples. After 100 cycles at 200 mA g^{-1}, the specific capacities of Fe_2O_3-500, Fe_2O_3-600 and Fe_2O_3-400 were maintained at 969, 838 and 722 mAh g^{-1}, respectively. As a comparison, the cubic Fe_2O_3 sample only delivers 445 mAh g^{-1} at 100 mA g^{-1} (Figure S6). The outstanding lithium storage capacities of Fe_2O_3-500 might be attributed to the unique structure, including stable micro-nano structure, high surface area and relatively suitable pore size.[39] Moreover, Figure 7e indicates that the Fe_2O_3-500 sample exhibits good cycle stability at various current rates. Specifically, the corresponding CE at the current density of 0.2 A g^{-1} is close to 100% and high capacities of 825 and 750 mAh g^{-1} are maintained after 50 cycles at current densities of 0.5 and 1 A g^{-1}, respectively. More impressively, the battery still shows outstanding cycle stability as the cycle increases. As shown in Figure S7, it retains a reversible capacity up to 707.4 mAh g^{-1}

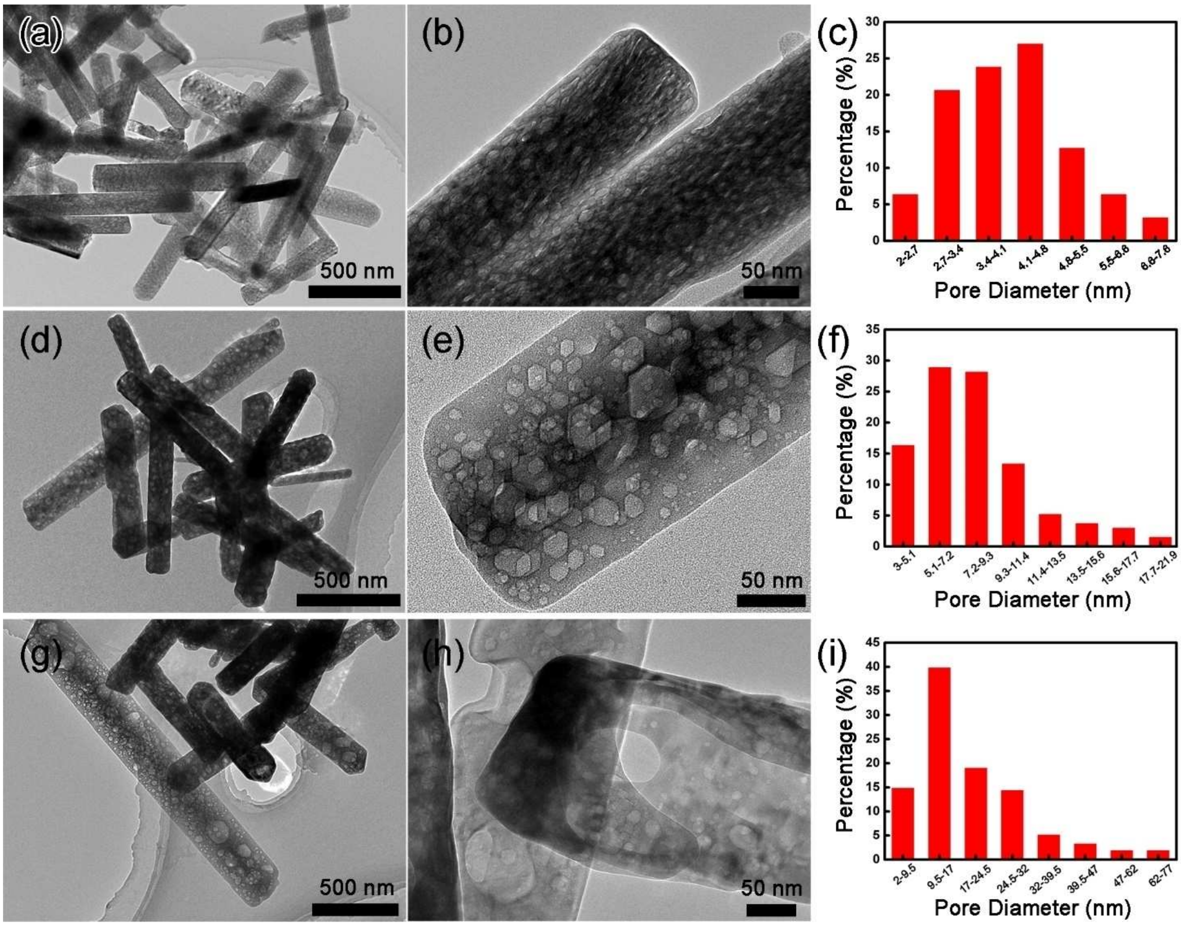

Figure 6. Typical TEM images of Fe_2O_3-400 (a, b), Fe_2O_3-500 (d, e), Fe_2O_3-600 (g, h). (c, f, i) the corresponding size distribution of the pores in Fe_2O_3 nanorods.

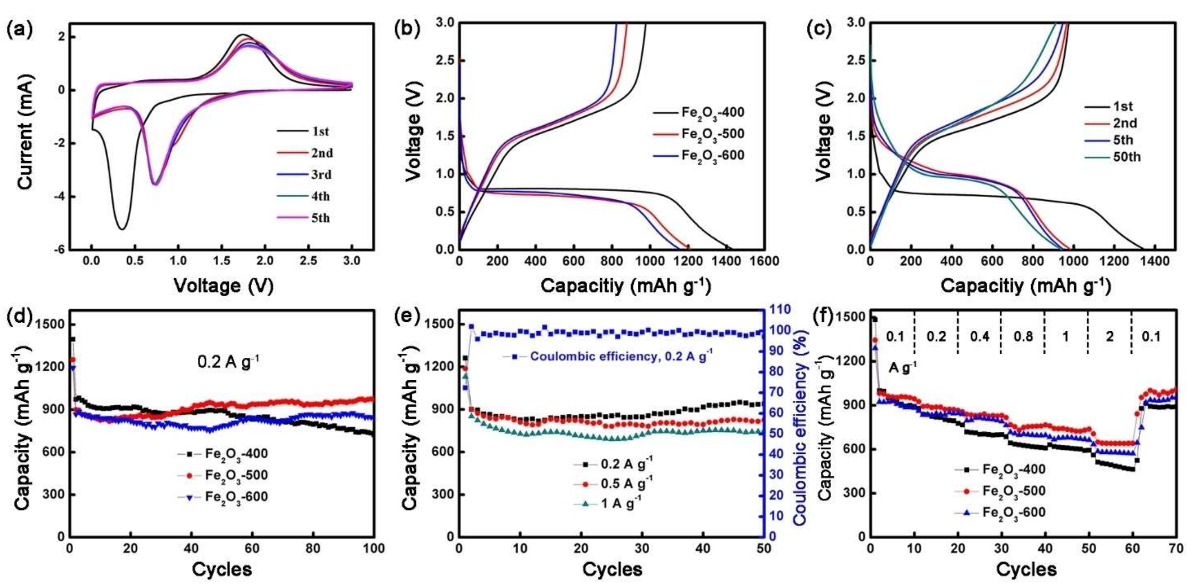

Figure 7. Electrochemical performance of samples. (a) CV curves of Fe_2O_3-500 sample at a scan rate of 0.5 mV s^{-1}. (b) initial charge/discharge profiles. (c) charge/discharge curves at 0.2 A g^{-1} for Fe_2O_3-500 electrode. (d) cycling performance of all the Fe_2O_3 electrodes at 0.2 A g^{-1}. (e) cycling performance at different current densities of Fe_2O_3-500 electrode. (f) rate capabilities.

after 200 cycles at 1 A g^{-1}. Furthermore, the Fe_2O_3-500 sample displays excellent rate capability. As demonstrated in Figure 7f, the capacity decreases slowly in the continuous cycling process as the current density increases. The Fe_2O_3-500 delivers a capacity of 640 mAh g^{-1} at 2 A g^{-1}, which is higher than the theoretical capacity (372 mAh g^{-1}) of graphite. After the current density returns to 0.1 A g^{-1}, the electrode shows a capacity of about 976 mAh g^{-1}. From Figure S8, it can be seen that cubic Fe_2O_3 only delivers discharge capacity of 257 mAh g^{-1} at 2 A g^{-1}, which is much lower than that of porous flute-like Fe_2O_3. The high reversible capacity of porous Fe_2O_3 can be attributed to its unique microstructure, which provides more reaction active sites with Li^+ and increases the utilization of active materials. The result indicates that the optimized porous structure can not only increase reversible capacity, but also improve the rate capability.

The long-cycling performances of three products were conducted at a current density of 2 A g^{-1}, as shown in Figure 8.

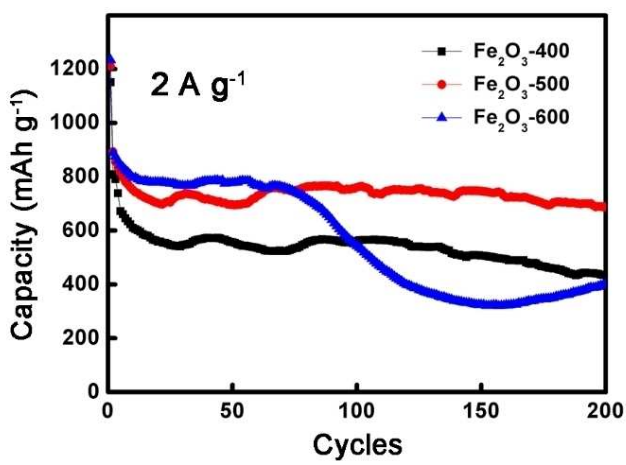

Figure 8. Cycling performances of Fe_2O_3-400, Fe_2O_3-500 and Fe_2O_3-600 at 2 A g^{-1}.

Compared to the Fe_2O_3-400 and Fe_2O_3-600 sample, the sample calcined at 500 °C possesses higher specific capacity and better stability. The specific capacity of Fe_2O_3-500 undergoes a trivial decrease during the first 50 cycles and maintains at 687.7 mAh g^{-1} in the subsequent cycles. The enhanced lithium storage performance can be attributed to the unique porous structure of the Fe_2O_3-500. The porous framework with a suitable pore size can efficiently alleviate the volume change and avoid the pulverization of active materials.[35,38]

Table 1 presents a comparison of electrochemical properties of porous Fe_2O_3 nanorods and the samples reported in literature. As can be seen from Table 1, Fe_2O_3 nanorods with optimized porosity are better in cyclic stability and rate capability than the samples reported in literature. Obviously, the porous structure contributes to the improvement of lithium storage properties.

To further understand the lithium storage performance of three different nanostructures, their transport kinetics was

Table 1. Comparison of electrochemical properties of porous Fe_2O_3 nanorods and the samples reported in literature.

Sample	Current density (mA g^{-1})	Cycle number	Specific capacity (mAh g^{-1})	Reference
Fe_2O_3 hollow spheres	200	100	710	[14]
Fe_2O_3 hollow cubic	100	100	457	[15]
porous Fe_2O_3 nanotubes	1000	25	613.7	[20]
porous flower-like α-Fe_2O_3	952	35	250	[30]
silver-incorporated Fe_2O_3-C porous microcubes	1000	700	538	[35]
rod-like porous Fe_2O_3@C	200	100	581	[34]
α-Fe_2O_3@carbon aerogel	100	50	581.9	[37]
Fe_2O_3-500 porous nanorods	200 1000 2000	100 200 200	969 707.4 687.7	This work

studied using electrochemical impedance spectra (EIS) measurements. The equivalent electrical circuit was also fitted according to impedance spectrum.[40] As exhibited in Figure 9, the Nyquist plots consist of two semicircles at high

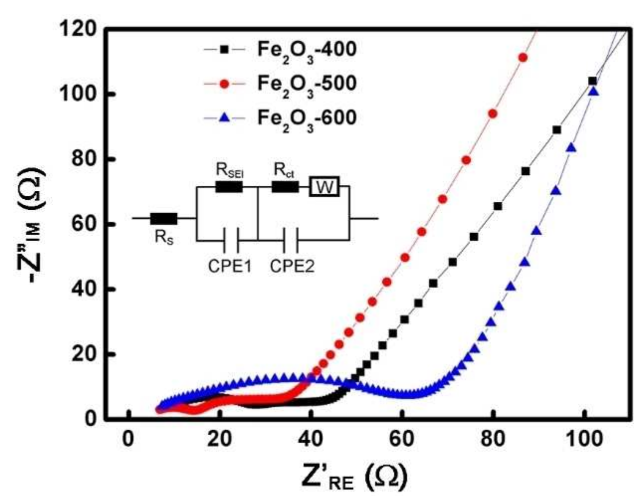

Figure 9. EIS of Fe_2O_3-400, Fe_2O_3-500 and Fe_2O_3-600 electrodes after 200 cycles, insert is the equivalent electrical circuit.

and medium frequency, and a straight line at low frequency. The first semicircle in the high frequency region represents the electrochemical resistance of SEI layer (R_{SEI}). The second semicircle in the medium frequency region corresponds to the charge transfer resistance through electrode/electrolyte (R_{ct}). The straight line at low frequency reflects the ionic resistance for the electrolyte-filled pores inside the electrode structures.[41] Obviously, the Fe_2O_3-500 electrode has a smaller resistance (R_{ct} = 25.6 Ω) compared with Fe_2O_3-400 (R_{ct} = 37.5 Ω) and Fe_2O_3-600 (R_{ct} = 62.5 Ω), suggesting the faster charge

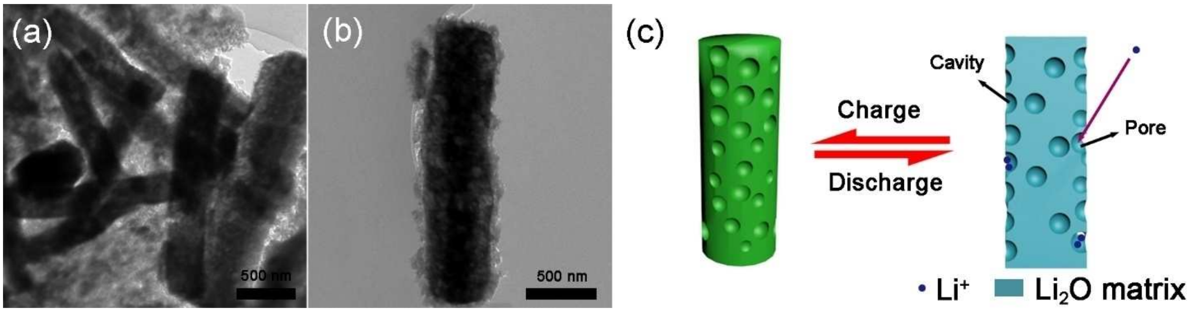

Figure 10. (a, b) TEM images of the Fe_2O_3-500 electrode after 50 cycles at a current density of 500 $mA\,g^{-1}$. (c) Schematic illustration of the charge/discharge process of Fe_2O_3 nanorods.

transfer kinetics among these samples. After 200 cycles, the Fe_2O_3-500 electrode shows relatively high electrical conductivity, which contributes to the improved lithium storage at high current density.

The microstructure of electrode was examined by TEM to investigate the porous framework stability. It can be seen from Figure 10a that the morphology of the Fe_2O_3 can be clearly observed and still maintains a rod shape. In some nanorods, pulverization inevitably takes place, resulting in the aggregation of the nanoparticles.[42] Figure 10b shows an enlarged TEM image of a single rod, where many mesopores can still be found. This feature indicates that the Fe_2O_3-500 possesses robust porous structure, which helps to improve the cycle performance. Based on the above results, the schematic illustration of the charge/discharge process of Fe_2O_3 electrode is shown in Figure 10c. The Fe_2O_3 nanorods contain a number of mesopores and cavities that serve as reservoirs for lithium ions and electrolyte. During the electrochemical cycling, these reservoirs efficiently accommodate huge volume change and shorten the path for Li ion diffusion. In addition, the robust porous framework is beneficial to the electron transportation and the formation of steady electrode/electrolyte interface, which provides great support in improved cycling performances.

Conclusions

In summary, flute-like Fe_2O_3 nanorods with tunable porosity are obtained by facile hydrothermal process and subsequent calcination. With the increase of annealing temperature, the pore size increases but the surface area decreases. Compared to the Fe_2O_3 annealed at 400 and 600 °C, the sample obtained at 500 °C exhibits good cycling stability and excellent high-rate capability (687.7 $mAh\,g^{-1}$ at 2 A g^{-1} after 200 cycles). The enhanced lithium storage performance can be attributed to combination effect of the optimized mesopore size and robust structural stability. On the one hand, a number of mesopores could generate much more active sites during Li insertion/extraction reactions and accommodate the volume change. On the other hand, an appropriate pore size distribution contributes to their structural stability. Furthermore, this work provides an effective way for the rational design of advanced electrodes with promising applications for LIBs.

Supporting Information Summary

The Supporting Information includes: Experiment section, the charecterization and electrochemical properties of cubic Fe_2O_3 and other associated figures.

Acknowledgements

The authors would like to thank the financial support from the National Natural Science Foundation of China (Grant Nos.: 10974105, 21701095), Natural Science Foundation of Shandong Province, China (Grant No.: ZR2017BEM007), Program of Science and Technology for Higher Education in Shandong Province, China (Grant No.: J17KA010), China Postdoctoral Science Foundation (Grant No.: 2017 M622131), and High-end Foreign Experts Recruitment Programs (Grant Nos.: GDW20163500110 and GDW20173500154). Y. Q. Wang would also like to thank the financial support from the Top-notch Innovative Talent Program of Qingdao City (Grant No.: 13-CX-08), the Taishan Scholar Program of Shandong Province, and Qingdao International Center for Semiconductor Photoelectric Nanomaterials and Shandong Provincial University Key Laboratory of Optoelectrical Material Physics and Devices.

Conflict of Interest

The authors declare no conflict of interest.

Keywords: lithium-ion batteries · Fe_2O_3 nanorods · anode materials · porosity

[1] B. Dunn, H. Kamath, J. M. Tarascon, *Science* **2011**, *334*, 928–935.
[2] J. B. Goodenough, K. S. Park, *J. Am. Chem. Soc.* **2013**, *135*, 1167–1176.
[3] G. D. Park, J. K. Lee, Y. C. Kang, *Adv. Funct. Mater.* **2017**, *27*, 1603399.
[4] V. Etacheri, R. Marom, E. Ran, G. Salitra, D. Aurbach, *Energy Environ. Sci.* **2011**, *4*, 3243–3262.
[5] X. L. Deng, Z. X. Wei, C. Y. Cui, Q. H. Liu, C. Y. Wang, J. M. Ma, *J. Mater. Chem. A* **2018**, *6*, 4013–4022.
[6] J. Wang, J. H. Tian, Naren, X. X. Wang, Z. W. Qin, Z. Q. Shan, *Energy Technol.* **2018**, *6*, 1913–1920.

[7] T. Yi, S. Yang, Y. Xie, *J. Mater. Chem. A* **2015**, *3*, 5750–5777.
[8] C. T. Kacica, L. S. Wang, T. S. Chadha, P. Biswas, *Energy Technol.* **2018**, *6*, 1966–1974.
[9] M. V. Reddy, T. Yu, C. H. Sow, Z. X. Shen, C. T. Lim, G. V. S. Rao, B. V. R. Chowdari, *Adv. Funct. Mater.* **2007**, *17*, 2792–2799.
[10] L. Zhang, H. B. Wu, X. W. Lou, *Adv. Energy Mater.* **2014**, *4*, 1300958.
[11] Q. Su, D. Xie, J. Zhang, G. Du, B. Xu, *ACS Nano* **2013**, *7*, 9115–9121.
[12] Q. L. Wei, F. Y. Xiong, S. S. Tan, L. Huang, E. H. Lan, B. Dunn, L. Q. Mai, *Adv. Mater.* **2017**, *29*, 1602300.
[13] S. H. Lee, Y. Noh, Y. Jo, Y. Kim, B. Kim, W. B. Kim, *Energy Technol.* **2018**, *6*, 1255–1260.
[14] B. Wang, J. S. Chen, H. B. Wu, Z. Wang, X. W. Lou, *J. Am. Chem. Soc.* **2011**, *133*, 17146–17148.
[15] H. Xiao, Y. Xia, W. K. Zhang, H. Huang, Y. P. Gan, X. Y. Tao, *J. Mater. Chem. A* **2013**, *1*, 2307–2312.
[16] F. C. Zheng, M. N. He, Y. Yang, Q. W. Chen, *Nanoscale* **2015**, *7*, 3410–3417.
[17] K. S. Lee, S. Park, W. Lee, Y. S. Yoon, *ACS Appl. Mater. Interfaces* **2016**, *8*, 2027–2034.
[18] T. Jiang, F. Bu, X. Feng, I. Shakir, G. Hao, Y. Xu, *ACS Nano* **2017**, *11*, 5140–5147.
[19] K. Z. Cao, L. F. Jiao, H. Q. Liu, Y. C. Liu, Y. J. Wang, Z. P. Guo, H. T. Yuan, *Adv. Energy Mater.* **2015**, *5*, 1401421.
[20] X. Cai, H. B. Lin, X. W. Zheng, X. Q. Chen, P. Xia, X. Y. Luo, X. X. Zhong, X. P. Li, W. S. Li, *Electrochim. Acta* **2016**, *191*, 767–775.
[21] M. C. Sun, M. F. Sun, H. X. Yang, W. H. Song, Y. Nie, S. N. Sun, *Ceram. Int.* **2017**, *43*, 363–367.
[22] X. D. Xu, R. G. Cao, S. Jeong, J. Cho, *Nano Lett.* **2012**, *12*, 4988–4991.
[23] X. Q. Zhang, B. He, W. C. Li, A. H. Lu, *Nano Research* **2018**, *11*, 1238–1246.
[24] Y. Kim, E. Choi, J. G. Kim, S. Lee, W. Yoon, M. H. Ham, W. B. Kim, *ChemElectroChem* **2017**, *4*, 2045–2051.
[25] X. Q. Zhang, W. C. Li, B. He, D. Yan, S. Xu, Y. L. Cao, A. H. Lu, *J. Mater. Chem. A* **2018**, *6*, 1397–1402.
[26] J. G. Kim, Y. Noh, Y. Kim, S. Lee, W. B. Kim, *Nanoscale* **2017**, *9*, 5119–5128.
[27] F. Granados-Correa, N. G. Corral-Capulin, M. T. Olguín, C. E. Acosta-León, *Chem. Eng. J.* **2011**, *171*, 1027–1034.
[28] Z. Y. Wang, D. Y. Luan, S. Madhavi, Y. Hu, X. W. Lou, *Energy Environ. Sci.* **2012**, *5*, 5252–5256.
[29] J. Liu D. Xue, *Adv. Mater.* **2008**, *20*, 2622–2627.
[30] T. R. Penki, S. Shivakumara, M. Minakshi, N. Munichandraiah, *Electrochim. Acta* **2015**, *167*, 330–339.
[31] Y. Y. Fu, R. M. Wang, J. Xu, J. Chen, Y. Yan, A. V. Narlikar, H. Zhang, *Chem. Phys. Lett.* **2003**, *379*, 373–379.
[32] Y. S. Wang, S. R. Wang, H. X. Zhang, X. L. Gao, J. D. Yang, L. W. Wang, *J. Mater. Chem. A,* **2014**, *2*, 7935–7943.
[33] H. G. Wang, Y. Q. Zhou, Y. Shen, Y. H. Li, Q. H. Zuo, Q. Duan, *Electrochim. Acta* **2015**, *158*, 105–112.
[34] Y. Sun, X. H. Liu, F. Z. Huang, S. K. Li, Y. H. Shen, A. J. Xie, *Mater. Res. Bull.* **2017**, *95*, 321–327.
[35] Q. Li, H. J. Wang, J. J. Ma, X. Yang, R. Yuan, Y. Q. Chai, *J. Alloys Compd.* **2018**, *735*, 840–846.
[36] D. Larcher, D. Bonnin, R. Cortes, I. Rivals, L. Personnaz, J. M. Tarascon, *J. Electrochem. Soc.* **2003**, *150*, A1643-A1650.
[37] D. W. Luo, F. Lin, W. D. Xiao, W. J. Zhu, *Ceram. Int.* **2017**, *43*, 2051–2056.
[38] C. C. Zhang, Y. H. Xu, W. Y. Chen, L. Y. Sun, D. H. Xu, Y. Yan, X. Y. Yu, *J. Electroanal. Chem.* **2018**, *816*, 114–122.
[39] S. J. Hao, B. W. Zhang, S. Ball, J. S. Wu, M. Srinivasan, Y. Z. Huang, *J. Mater. Chem. A* **2016**, *4*, 16569–16575.
[40] T. Xin, F. Y. Diao, C. Li, H. L. Feng, G. J. Liu, J. J. Zou, Y. H. Ding, B. Liu, Y. Q. Wang, *Mater. Res. Bull.* **2018**, *99*, 196–203.
[41] S. M. Xu, C. M. Hessel, H. Ren, R. B. Yu, Q. Jin, M. Yang, H. J. Zhao, D. Wang, *Energy Environ. Sci.* **2014**, *7*, 632–637.
[42] L. Zhou, Z. H. Zhuang, H. H. Zhao, M. T. Lin, D. Y. Zhao, L. Q. Mai, *Adv. Mater.* **2017**, *29*, 1602914.

Submitted: February 13, 2019
Accepted: March 18, 2019